

## Numerical Simulation of the Thermal Performance of a Tubular Solar Air Heater

Yousif Fateh Midhat<sup>1,\*</sup>, Issam Mohammed Ali Aljubury<sup>2</sup>

Department of Mechanical Engineering, College of Engineering, University of Baghdad, Baghdad, Iraq  
[yousif.midhat1403m@coeng.uobaghdad.edu.iq](mailto:yousif.midhat1403m@coeng.uobaghdad.edu.iq)<sup>1</sup>, [drissam@uobaghdad.edu.iq](mailto:drissam@uobaghdad.edu.iq)<sup>2</sup>

### ABSTRACT

In this work, a flat-plate solar air heater (FSAH) and a tubular solar air heater (TSAH) were designed and tested numerically. The work investigates the effect of increasing the contact area between the flowing air and the absorber surface of each heater and predicts the expected results before the fabrication of the experimental rig. Three-dimensional two models were designed and simulated by the ANSYS-FLUENT 16 Program. The solar irradiation and ambient air temperature were measured experimentally on December 1<sup>st</sup> 2022, at the weather conditions of Baghdad City- Iraq, at three air mass flow rates, 0.012 kg/s, 0.032 kg/s, and 0.052 kg/s. The numerical results showed the advantage in the thermal performance of the TSAH in comparison to the FSAH, represented by better air temperature difference, better heat transfer from the absorber to air, and better thermal efficiency. The TSAH has a higher thermal efficiency than the FSAH by 7 %, 19 % °C, and 22 % at 0.012 kg/s, 0.032 kg/s, and 0.052 kg/s, respectively. The improvement of the thermal characteristics of the TSAH can be referred to as the increment in the heat transfer contact area between the absorber and the flowing air.

**Keywords:** Numerical simulation, Thermal performance, Flat-plate solar air heater, Tubular solar air heater.

---

\*Corresponding author

Peer review under the responsibility of University of Baghdad.

<https://doi.org/10.31026/j.eng.2023.11.09>

This is an open access article under the CC BY 4 license (<http://creativecommons.org/licenses/by/4.0/>).

Article received: 01/03/2023

Article accepted: 22/10/2023

Article published: 01/11/2023

## المحاكاة العددية للاداء الحراري لسخان هواء شمسي انبوبي

يوسف فاتح مدحت<sup>1\*</sup>، عصام محمد علي الجبوري<sup>2</sup>

قسم الهندسة الميكانيكية، كلية الهندسة، جامعة بغداد، بغداد، العراق

### الخلاصة

في الدراسة الحالية، سخان هواء ذو سطح ماص مستوي (FSAH)، و سخان هواء ذو سطح ماص انبوبي (TSAH) تم تصميمهما و محاكاة سلوكيهما الحراريين عدديا. يتضمن البحث دراسة تأثير زيادة مساحة التلامس بين السطح الماص و الهواء المتدفق على اداء السخان الشمسي يتم التنبؤ بالاداء الحراري لكل سخان قبل تصنيعه عمليا. نموذجان ثلاثيا الابعاد للسخانين الحراريين تم تصميمهما و محاكاة سلوكهما بواسطة برنامج فلونت- أنسس 16. تم قياس الاشعاع الشمسي و درجة حرارة الهواء الداخل لكل جهاز عمليا عند الاول في كانون الاول 2022، حسب الظروف الجوية لمدينة بغداد- العراق. عند ثلاث معدلات تدفق للهواء 0,012 كغ/ثا ، 0.032 كغ/ثا ، 0,052 كغ/ثا . اظهرت النتائج النظرية تفوق السخان الانبوبي على السخان المسطح من حيث تسخين الهواء بشكل افضل، اذ كانت 31، 36، 52 °س عند السخان المسطح، و 42، 58، 35 °س عند السخان الانبوبي ، عندما كان معدل تدفق الهواء 0,012 كغ/ثا ، 0.032 كغ/ثا ، 0,052 كغ/ثا، بالتتابع. كانت قيم الكفاءة الحرارية للسخان الانبوبي اعلى من اقرانها عند السخان المسطح 7 %، 19 %، و 22 % ، عندما كان معدل تدفق الهواء 0,012 كغ/ثا ، 0.032 كغ/ثا ، 0,052 كغ/ثا بالتتابع.

**الكلمات المفتاحية:** محاكاة عددية ، اداء حراري ، سخان هواء شمسي مسطح ، سخان هواء شمسي انبوبي.

## 1. INTRODUCTION

In general, a solar air heater (SAH) is a device employed to transfer solar energy to the flowing air. Today, Energy providing has taken significant attention. Access to clean energy is important for social and economic growth (Amori and Zghair, 2019). In the last decades, energy sources that are sustainable and renewable have been employed in a variety of applications, like solar energy. Solar-absorbing systems of simple designs and accepted thermal efficiency, such as solar air heaters (Shbailat and Jassim, 2018; Jassim and Shbailat, 2018), are frequently used. Like other systems, SAHs have some drawbacks, like the low heat transfer between the air and the absorber surface, low heat capacity of air, and energy losses (Farhan and Sahi, 2016). The researchers reviewed many efforts to reduce these losses and increase SAH's efficiency as follows:

(Ammari, 2003) designed a mathematical model for calculating the thermal performance of a single-pass flat-plate solar air collector. The mathematical model was built to determine the effect of the addition of metal slats on the efficiency of the solar collector. The predicted temperature and efficiency of the two air heaters were shown, and it was found that the performance of the modern model heater with the slats was significantly better than that of the



most common type heater. **(Varol and Oztop, 2008)** dealt with numerical analysis of the natural convection heat transfer inside two inclined solar collectors, they observed that the flow and performance are affected by the shape of the collector, and also, heat transfer rate increases in the case of wavy enclosure than that of the flat enclosure. The mean Nusselt number was 15 and 16 at the flat and wavy absorbers. **(Olczak and Olek, 2016)** Examined how the assembly of evacuated tubes can affect the amount of heat lost. In the research, pipes with parabolic glass mirror reflectors and aluminum fins were chosen for the examination. Numerical techniques were used to analyze how the location of the fins concerning the direction of solar radiation affected the amount of the lost heat, and it was determined that the lost heat did not exceed 2.5 % of the energy absorbed. In the case of the direction opposite to the Sun, a temperature of more than 480 K was observed.

**(Sahu and Prasad, 2017)** set a computational fluid Dynamics (CFD) on an SAH's heat transfer and friction factor with circular ribs and different relative gap widths. The related Nusselt number and friction factor for the circular ribs were found to be more than that of smooth ribs. Nu Number was higher by 3.8 % for the ribbed plate, and the average friction factor was higher by 3.92% for the ribbed plate than the smooth plate. **(Alawy et al., 2018)** adopted a solar collector with a circular shape, the results showed that at increasing the inclination of the glass cover of the collector from 0-8.5°, hot air temperature at the outlet of the SAH increased from 134 °K to 141 °K, respectively. Numerical research was done to determine the impact of a helical channel on the efficiency of the SAH **(Heydari and Mesgarpour, 2018)**. The findings revealed that vortexes occasionally occur inside the air heater, and pressure drops with the increased heat exchange. The results indicate that the average thermal efficiency of a double-pass solar air heater with a helical channel is estimated to be 14.7% higher than a simple duct. **(Nasir, 2019)** employed plastic tubes as a flat plate solar collector's absorber to heat water, the difference in output temperature between the computational and experimental results was 4.2%, earlier review showed the ability of the CFD programs the predict the outcomes before the constructing of experimental models, the results showed improvement in input-output temperature difference was 3.1 °C, the maximum collector efficiency is 79%, and the maximum temperature is 67 °C. **(Jin et al., 2019)** studied the heat transfer process and flow properties of an SAH roughened with several V-shaped ribs, heat transmission was significantly improved due to the used ribs. The highest possible thermo hydraulic performance factor was 2.35 at a span wise rib number of 7, inclination angle of 45°, and channel height of 25 mm. **(Khanlari et al., 2020)** investigated how incorporating plus-shaped baffles inside solar air collectors may affect their performance in a drying process. The results of the experiments showed that the thermal efficiencies fall somewhere in the range of 62.11 % to 75.11 %. **(Singh, 2020)** investigated the effect of a porous serpentine wavy wire-mesh packed bed on SAH's thermal performance. According to the numerical data, there was an increase of 24.33 % in the thermohydraulic performance compared with SAH made with a flat absorber. **(Tuncer et al., 2020)** fabricated, and compared v-groove SAHs, with a parallel-pass and a double-pass. According to the findings, the average thermal efficiency for and was between 54 % and 78.18. **(Hussein et al., 2023)** examined how a double-pass SAH's thermal performance changes if a novel solar absorber was used. The first design had a flat plate solar absorber; the second one had a tubular absorber with a double pass fitted parallel to the airflow's direction. The second setup was 9.8% more efficient than the first. **(Midhat and Aljubury, 2023)** investigated the thermohydraulic performance of a tubular solar heater's tubular absorber, its efficiency

reached 81 % compared to 59% in the case of a flat solar heater. SAH's performance is the subject of many investigations to improve its efficiency by various enhancing methods. It has come to our attention that the efficiency of the selected tubular SAH was not investigated yet. Within the scope of this study, thermal-hydrodynamic behavior within a TSAH in Baghdad was analyzed through numerical simulation using ANSYS-FLUENT 16.0. Numerical simulation of an FPSAH and TSAH was performed via two three-dimensional models. The goal of this research is to show the heat transfer process that occurs through both of the two modelled SAHs before manufacturing them experimentally.

## 2. NUMERICAL MODELLING

**Fig. 1** shows a CAD of the conventional FSAH with its operation principle. A newly used annular aluminum cross-section tube consists of an inner circular tube surrounded by two jackets and separated by two longitudinal grooves. The two grooves allow solar rays to irradiate the inner tube. At the same time, the two lateral jackets receive solar irradiation, as shown in **Fig. 2**.

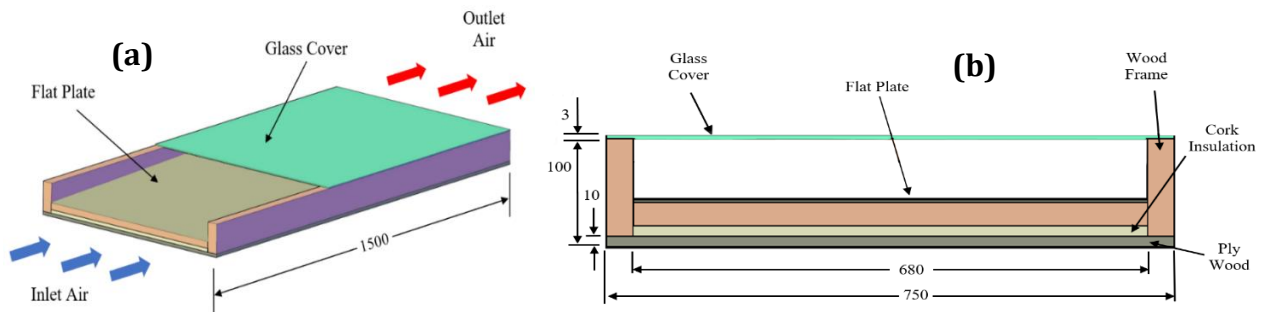


**Figure 1.** Schematic CAD of the FSAH, (a) ISO View, (b) Air inlet section.

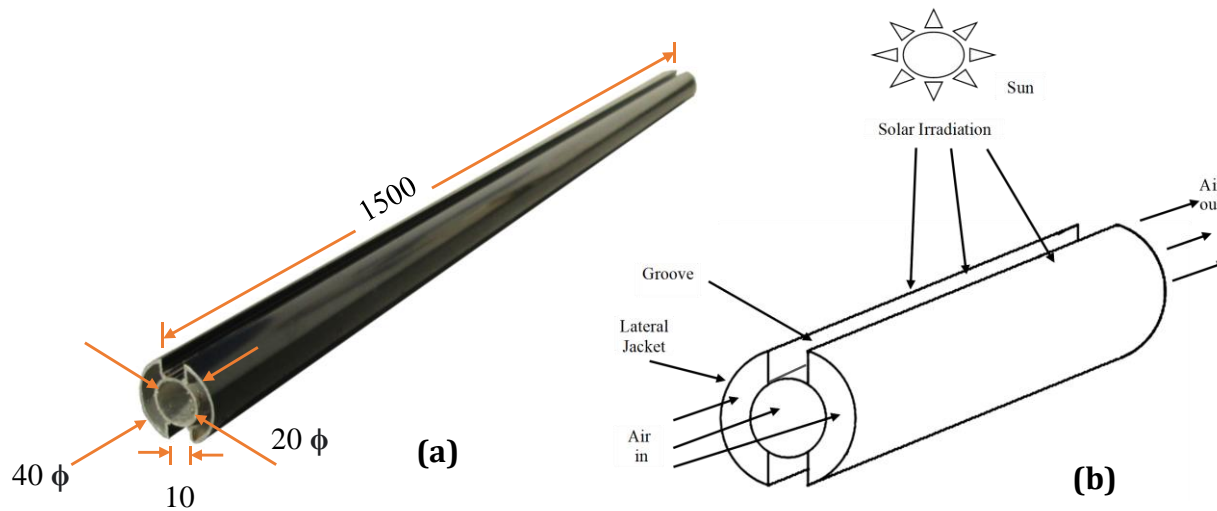


**Figure 2.** The pipe used in the TSAH, (a) with dimensions and (b) work principle .

The used tube in the TSAH is expected to work on heating the flowing air inside the inner tube better than using a flat plate as an absorber due to its larger contact area with air. **Fig. 3** shows a CAD of the TSAH, with dimensions and work principles.

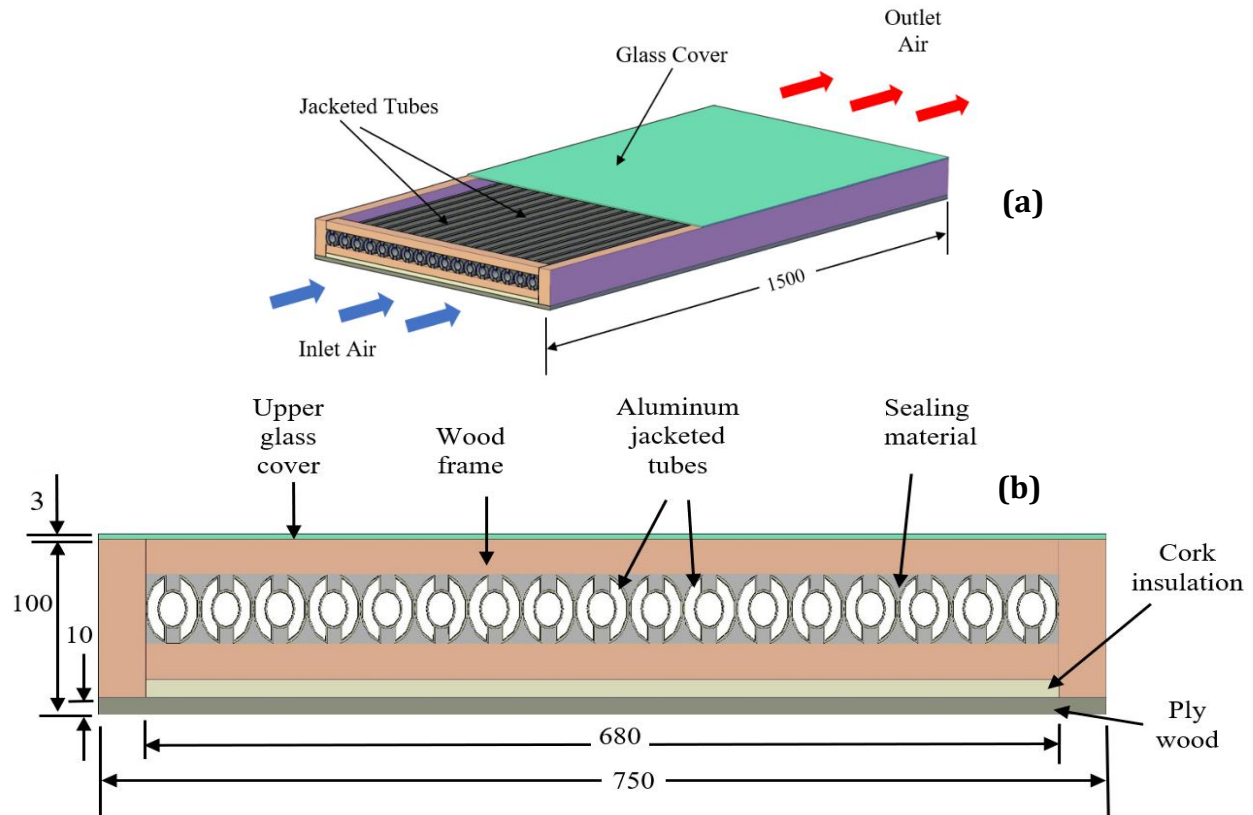


**Figure 3.** Schematic CAD of the TSAH, (a) ISO View, (b) Air inlet port.

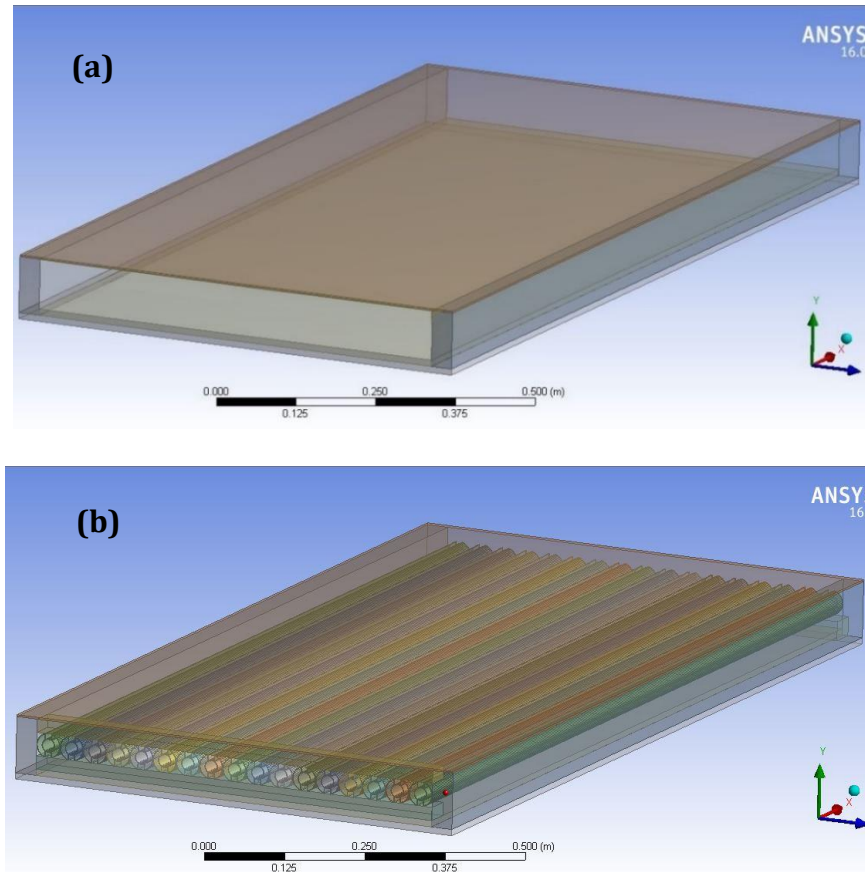
Two Numerical models were created to perform the necessary simulation, one for the FSAH, shown in **Fig. 4 (a)**, and the second belongs to the TSAH, as demonstrated in **Fig. 4 (b)**. The modelling was achieved using design modeler software equipped with a (fluent) program.

### 3. FLOW MODELS

K-epsilon turbulence model was tested on previous solar air collector models. k-epsilon model is a semi-empirical model based on phenomenological and practical considerations. It is the most widely used model for turbulent flows due to its precision and robustness and relatively low computation time cost. Re-Normalization group (RNG) method was used for developing the equations. Also, eddy viscosity was specified at 0.001 (**Hasan, 2018**). The pressure-based solver was selected (**Raj et al., 2020**).

#### 4. MESH GENERATION

For the simulation, the regions of boundary layers flow required enough nodes to sense the boundary effect and temperatures. Adding additional nodes to the mesh increases the time and computational requirements without adding extra sensible resolution. Therefore, a fine mesh has been used as enough nodes in the zones adjacent to the absorbers to capture the required suitable details of the fluid flow and heat transfer (**Amori and Zghair, 2019**). The computational domain of the SAHs is meshed using tetrahedron elements type (**Olczak and Olek, 2016**). Surface sizing is used to inflate the mesh by picking domain surfaces. An

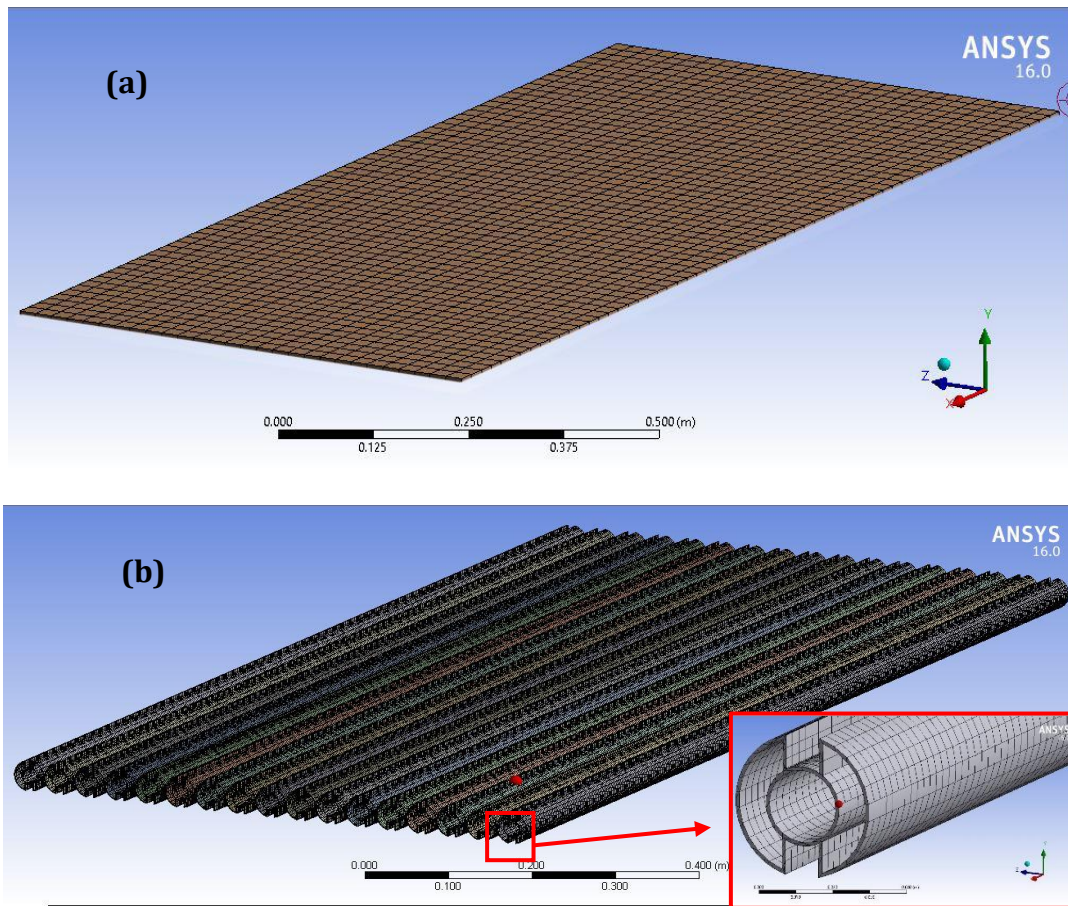


**Figure 4.** Geometry Models, (a) FSAH, (b) TSAH

appropriate biasing and biasing factor are used to generate finer mesh near the wall with an increasing growth rate of the boundary layer (**Singh, 2020**). The developed mesh properties are shown in **Table 1**. **Figs. 5 and 6** show the 3-D mesh generated in this work for two models of the SAHs.

**Table 1.** Generated mesh details

Display Style	Body Color	Relevance Center	Medium
Physics Preference	CFD	Initial Size Seed	Active Assembly
Solver Preference	Fluent	Smoothing	Medium
Relevance	51	Transition	Slow
Use Advanced Size Function	On: Curvature		

**Figure 5.** SAHs Meshed Absorbers: (a) FSAH, (b) TSAH

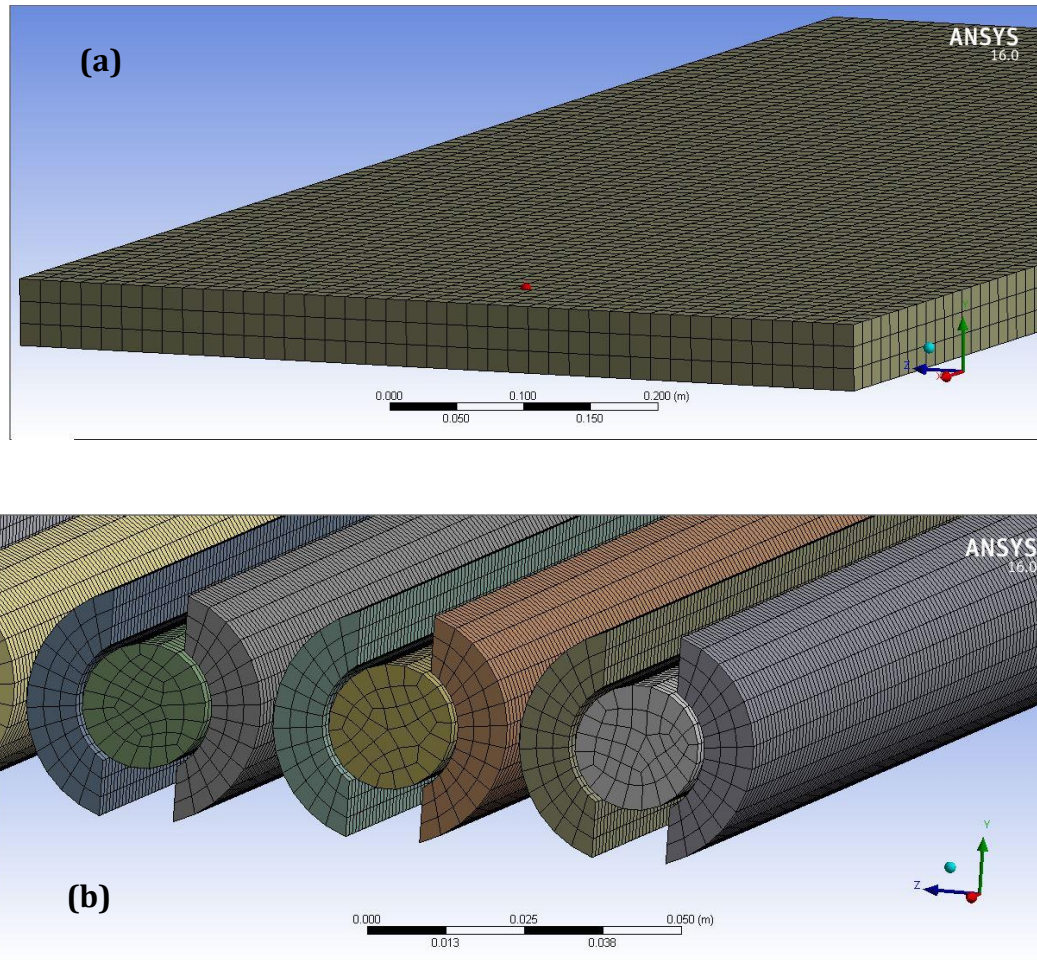


**Figure 6.** Fluid domain inside the modelled SAHs: (a) FSAH, (b) TSAH.

## 5. MATERIALS PROPERTIES

Air, aluminum, and glass were the materials that were chosen for the simulations. The selected materials have been chosen from **(Jassim and Shbailat, 2017)** to match the numerical work. In the materials database list, Air, aluminum, and glass properties were set to their default values and summarized in **Table 2**.

**Table 2.** Properties of Materials (ANSYS FLUENT 16.0)

Materials	Density (kg/m <sup>3</sup> )	Specific heat (J/kg.°k)	Thermal conductivity (W/m. °k)
Glass	2321	750	1.15
Aluminum	2.70	903	251
Air	1.29	1005	0.025



## 6. BOUNDARY CONDITIONS

Boundary conditions were assumed (**Al-Abbas, 2017**). **Fig. 7** shows the application of the boundary conditions and explains them as follows:

**Inlet Air:** Mass flow rate inlet boundary condition type has been defined. The inlet air temperature changed according to the experimental measurement. Air enters the solar collector at a temperature equal to the ambient temperature. Inlet boundary condition. The velocity and temperature of the collector inlet are given as:

At  $x = 0$  :

$$v = w = 0 \quad (1)$$

$$T_{in} = T_{ambient} \quad (2)$$

**Outlet Air:** Mass flow rate outlet boundary condition type has been defined at the air outlet port. The outlet of the solar collector is exposed to atmospheric pressure;

At  $x = L$

$$P_{out} = 101.325 \text{ kPa}$$

**Walls:** Glass cover was considered to be applied to heat flux. The walls between the absorber and air have been assumed (Coupled Thermal Walls) (**Hasan, 2017**) to enable the transmission of heat between them. Lateral and back wooden walls were given an adiabatic thermal condition by giving each one zero heat flux. The external surface of the solar collector is subjected to the boundary conditions of radiation and wind convection. At the absorber:

$$k_{abs.} \left( \frac{\partial T}{\partial n} \right)_{wall} = h(T_{air} - T_{abs.}) + \varepsilon_g \sigma (T_{sky}^4 - T_{abs.}^4) + I \quad (3)$$

where:

$k_{abs}$  is the conductivity of the absorber.

$h$  is the heat transfer coefficient between air and the absorber.

$T_{abs.}$  is the temperature of the absorber.

$\varepsilon_g$  is the emissivity of the glass.

$T_{sky}$  is the sky temperature.

$I$  is solar irradiation.

At the frame, there is no slip or flow.

$$u = v = w = 0 \quad (4)$$

The glass surface is exposed to constant heat flux  $q''$  and transmissive to the absorber, such that:

$$\frac{\partial T}{\partial n} = \frac{q''}{k_{abs}} = \frac{I\tau\alpha}{k_{abs}} \quad (5)$$

$\alpha$  is the absorber plate absorptivity.  $\tau$  is the absorber glass transmissivity.  $k$  is the absorber plate's thermal conductivity.

At the back surface and others, all sides of the air solar collector are taken as insulated surfaces such that:

$$\frac{\partial T}{\partial n} = 0 \tag{6}$$

where  $n$  is the normal unit vector on the absorber

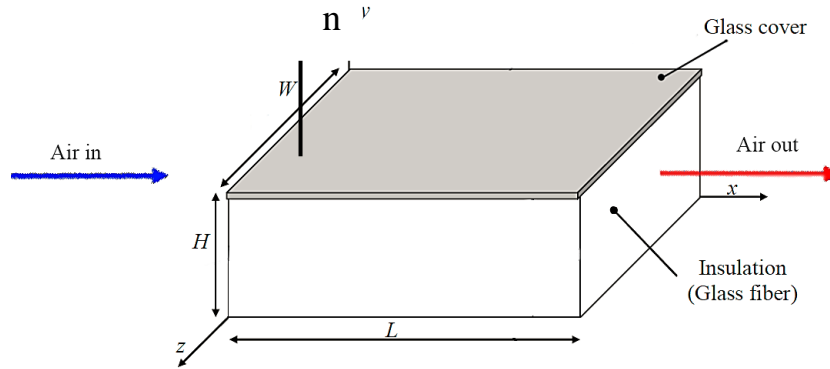


**Figure 7.** Schematic diagram of the boundary conditions.

## 7. GOVERNING EQUATIONS

The finite volume technique is based on the program to solve the governing equations of forced convection (**Hammadi, 2015**). The governing equations of continuity, momentum, and energy and turbulence model for the fluid region can be expressed as detailed below:

### 7.1 Continuity Equation

The continuity equation for air, as an incompressible fluid, can be formed as (**Yasin and Ghanim, 2017**):

$$\frac{\partial(\rho u)}{\partial x} + \frac{\partial(\rho v)}{\partial y} + \frac{\partial(\rho w)}{\partial z} = 0 \tag{7}$$

where  $u, v, w$  are air velocity (m/s) units in the directions  $x, y, z$ , respectively.  
 $\rho$  is the density of air ( $\text{m}^3/\text{s}$ ).

### 7.2 Momentum Equations

The momentum equations were obtained from (**Salih et al., 2020**):

In  $x$ -direction:

$$u \frac{\partial u}{\partial x} + v \frac{\partial u}{\partial y} + w \frac{\partial u}{\partial z} = -\frac{1}{\rho} \frac{\partial p}{\partial x} + (v + v_t) \left[ \frac{\partial^2 u}{\partial x^2} + \frac{\partial^2 u}{\partial y^2} + \frac{\partial^2 u}{\partial z^2} \right] \tag{8}$$

In  $y$ -direction:



$$u \frac{\partial v}{\partial x} + v \frac{\partial v}{\partial y} + w \frac{\partial v}{\partial z} = -\frac{1}{\rho} \frac{\partial p}{\partial y} + (v + \nu_t) \left[ \frac{\partial^2 v}{\partial x^2} + \frac{\partial^2 v}{\partial y^2} + \frac{\partial^2 v}{\partial z^2} \right] \quad (9)$$

In z-direction:

$$u \frac{\partial w}{\partial x} + v \frac{\partial w}{\partial y} + w \frac{\partial w}{\partial z} = -\frac{1}{\rho} \frac{\partial p}{\partial z} + (v + \nu_t) \left[ \frac{\partial^2 w}{\partial x^2} + \frac{\partial^2 w}{\partial y^2} + \frac{\partial^2 w}{\partial z^2} \right] \quad (10)$$

$\nu_t$  is the turbulent kinematic viscosity, related to  $k$  and  $\epsilon$  by the expression from **(Salman and Nima, 2019)**.

$$\nu_t = C_\mu \frac{k^2}{\epsilon_{air}} \quad (11)$$

where:

$C_\mu$  is a model constant =0.09 **(Jouybari and Lundström, 2020)**

$k$  is the thermal conductivity of the absorber.

$\epsilon_{air}$  is the dissipation rate, taken unity **(Kundan, 2017)**.

### 7.3 Energy Equation

The momentum equations were obtained from **(Hussain and Mustafa, 2010)**:

$$\left[ u \frac{\partial T}{\partial x} + v \frac{\partial T}{\partial y} + w \frac{\partial T}{\partial z} \right] = \left( \frac{\nu}{Pr} + \frac{\nu_t}{\sigma} \right) \left[ \frac{\partial^2 T}{\partial x^2} + \frac{\partial^2 T}{\partial y^2} + \frac{\partial^2 T}{\partial z^2} \right] = 0 \quad (12)$$

where:

$\nu$  is the kinematic viscosity ( $m^2/s$ ),  $\nu_t$  is the kinematic turbulent viscosity ( $m^2/s$ ),  $Pr$  is Prandtl number,  $\sigma$  is the surface tension (N/m)

### 7.4 Turbulence Model Equation

The turbulence model is related to Reynolds stresses tensor to close the system of mean turbulent flow equations. The different models as a model of realizable k-epsilon, Renormalize Group k-epsilon (RNG) model, Standard k-epsilon, and shear stress transport k-Omega (SST) were tested. The k-epsilon model is a semi-empirical model based on phenomenological considerations and empiricism. It is the most widely used model for turbulent flows due to the precision and robustness of this model also the relatively low cost in computation time. The Re-Normalization group (RNG) method was used for developing the k-epsilon model to renormalize equations of Navier-Stoke. Also, the eddy viscosity is specified in the k-epsilon model from a single turbulence length scale, so the turbulent diffusion is determined.  $k - \epsilon$  model is by far the most widely popular turbulence model used in this field, such as the work of **(Kadhim and Al Thamiry, 2021)** and many more. It is a semi-empirical model and includes two transport equations, the first one for specific turbulent kinetic energy ( $k$ ) and the second for the turbulent dissipation rate ( $\epsilon$ ); their relations were obtained as **(Hussein et al., 2023)**.



$$\begin{aligned} \frac{\partial}{\partial x}(\rho u K') + \frac{\partial}{\partial y}(\rho v K') + \frac{\partial}{\partial z}(\rho w K') = \frac{\partial}{\partial x} \left[ (\mu + \mu_t) \frac{\partial K'}{\partial x} \right] & \quad (13) \\ & + \frac{\partial}{\partial y} \left[ (\mu + \mu_t) \frac{\partial K'}{\partial y} \right] + \frac{\partial}{\partial z} \left[ (\mu + \mu_t) \frac{\partial K'}{\partial z} \right] \end{aligned}$$

$$\begin{aligned} \frac{\partial}{\partial x}(\rho u \varepsilon) + \frac{\partial}{\partial y}(\rho v \varepsilon) + \frac{\partial}{\partial z}(\rho w \varepsilon) = \frac{\partial}{\partial x} \left[ (\mu + \mu_t) \frac{\partial \varepsilon}{\partial x} \right] & \quad (14) \\ & + \frac{\partial}{\partial y} \left[ (\mu + \mu_t) \frac{\partial \varepsilon}{\partial y} \right] + \frac{\partial}{\partial z} \left[ (\mu + \mu_t) \frac{\partial \varepsilon}{\partial z} \right] \end{aligned}$$

where  $\mu$  is the viscosity of air (Pa.s),  $\mu_t$  is the turbulence viscosity of air (Pa.s).

The turbulent kinetic energy equation is obtained from **(Salih and Najim, 2019)** as follows:

$$\begin{aligned} K' = \mu_t \left[ 2 \left( \frac{\partial u}{\partial x} \right)^2 + 2 \left( \frac{\partial v}{\partial y} \right)^2 + 2 \left( \frac{\partial w}{\partial z} \right)^2 \right. & \quad (15) \\ & \left. + \left( \frac{\partial u}{\partial y} + \frac{\partial v}{\partial x} \right)^2 + \left( \frac{\partial w}{\partial y} + \frac{\partial v}{\partial z} \right)^2 + \left( \frac{\partial w}{\partial x} + \frac{\partial u}{\partial z} \right)^2 \right] \end{aligned}$$

## 8. SOLUTION METHOD

(SIMPLE) algorithm was selected for pressure-velocity coupling as it numerically solves the Navier-Stokes equation. At the same time, a second-order discretization of momentum and energy equations was used **(Jehhef, 2018)**. For turbulent kinetic energy and turbulent dissipation rate, the first-order equation was used **(Jouybari and Lundström, 2020)**. Under-Relaxation factors of solution controls were set to their default values **(Raj et al., 2020)**. Standard, relative to cell zone solution, has been selected at the solution initialization **(Nakhla, 2013)**. A flow solution ended up with a convergence of the residuals to  $10^{-4}$ ; they required (30 to 120) iterations. The computing time of the model simulations for one case was about one to ten hours, depending on the case.

## 9. GRID INDEPENDENCE TEST

Any CFD simulation cannot be trusted unless a grid independence test (GIT) is done to ensure whether the result depends on the grid. The output result from coarser or finer mesh is not the same, so the mesh needs to be varied to reach the accepted tolerance level. This process is done by varying the mesh size from course to finer form and then checking the output result from each mesh. When varying (smoothing), the mesh does not affect the results much. The test can be stopped and depend on the last minimum mesh size reached in the final solution output. GIT can be done using the parametric analysis after setting input and output parameters, meshing, and comparing the results of various mesh sizes from course to fine with the solution output. First, the default mesh was generated to check if the studied domain can be meshed or if the geometry has any error. Nodes and elements of mesh details were assigned to be reviewed later. The temperature was set as the output parameter. To ensure the solution independency of the generated mesh, four different mesh sizing were tested to get the corresponding number of



elements, as shown in Fig. 7. The results show that the last sizing of 1344000 mesh nodes and 1403246 mesh elements is the most suitable case as it represents an accepted compromising between the solution’s accuracy and solution time.

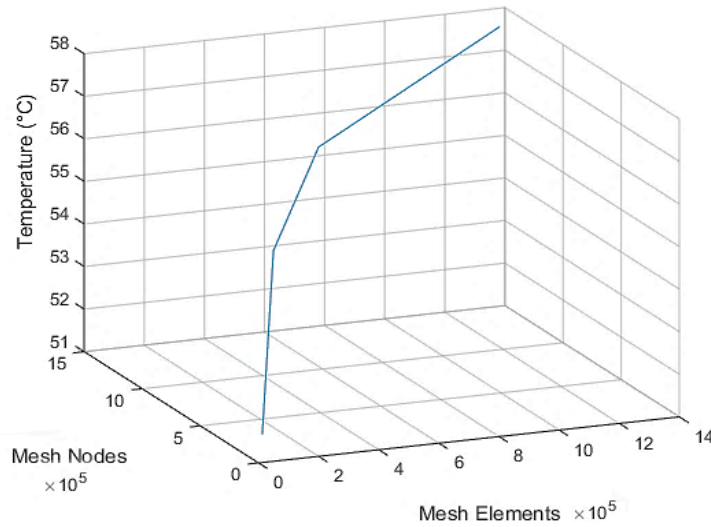


Figure 7. Grid Independence Test

### 10. DATA REDUCTION

The incident thermal power depends on the intensity of incident solar irradiation on the collector surface and the absorber’s area.

The incident thermal power on the SAH is calculated (Kalogirou, 2014):

$$Q_{in} = I \times A_{abs} \tag{16}$$

where:

*I* is the solar irradiation on SAH’s surface.

*A<sub>abs</sub>* is the area of the absorber’s surface.

Thermal power transferred to air (*Q<sub>gain</sub>*) is calculated by (Duffie, 1985) :

$$Q_{gain} = \dot{m} \cdot C_p \cdot \Delta T \tag{17}$$

It is required to calculate the mass flow rate of the passing air (*m*) by:

$$\dot{m} = \rho \cdot V \cdot A_c \tag{18}$$

where:

*ρ* is the density of air (1.2 kg/m<sup>3</sup>).

*V* is the velocity of air within the SAH

*A<sub>c</sub>* is the area of the cross-section

*ΔT* is the temperature difference of air (°C) between inlet port and outlet port

The thermal efficiency is calculated as the following formula (Çengel, 2004):

$$\eta_{th} = \frac{Q_{gain}}{Q_{in}} \quad (19)$$

## 11. RESULTS AND DISCUSSIONS

**Figs. 8 to 10** show the temperature contours of the three absorbers after the simulation at noon with three experienced air flow rates. The figures revealed that the maximum absorber temperature belongs to the FPSAH, followed by the TSAH. Also, temperature contours grow early at the flat absorber compared to the other two absorbers at any specific air flow rate.

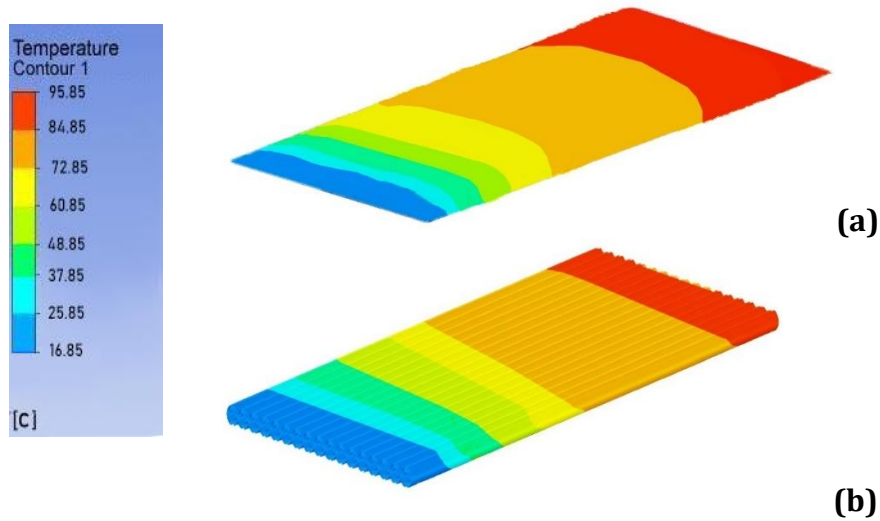


**Figure 8.** Absorber temperature at 0.012 kg/s air flow rate of (a) FSAH and (b) TSAH.

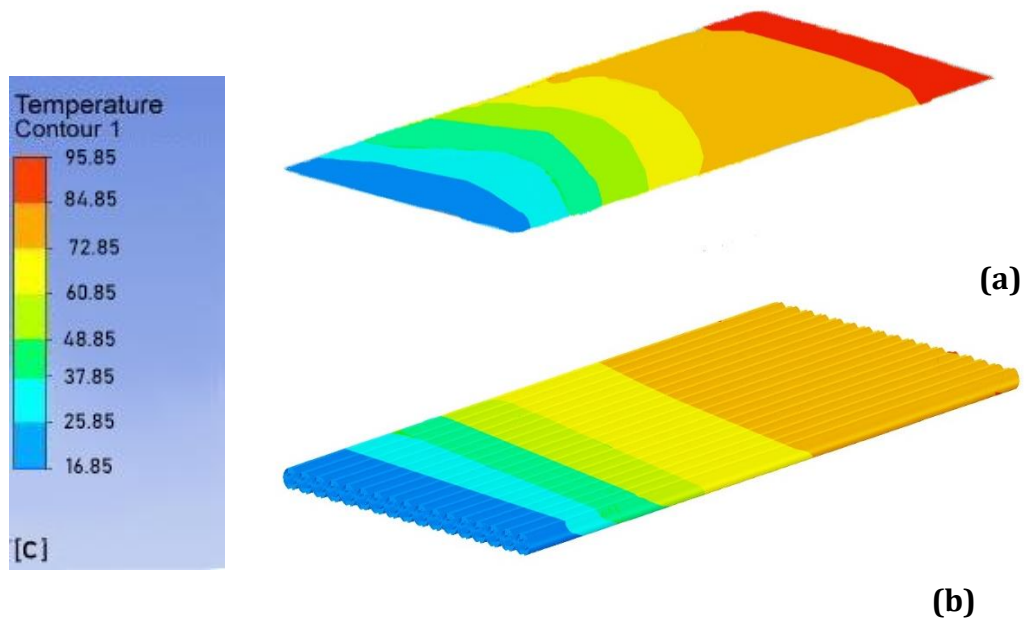


**Figure 9.** Absorber temperature at 0.032 kg/s air flow rate of the FSAH (a) and the TSAH (b).

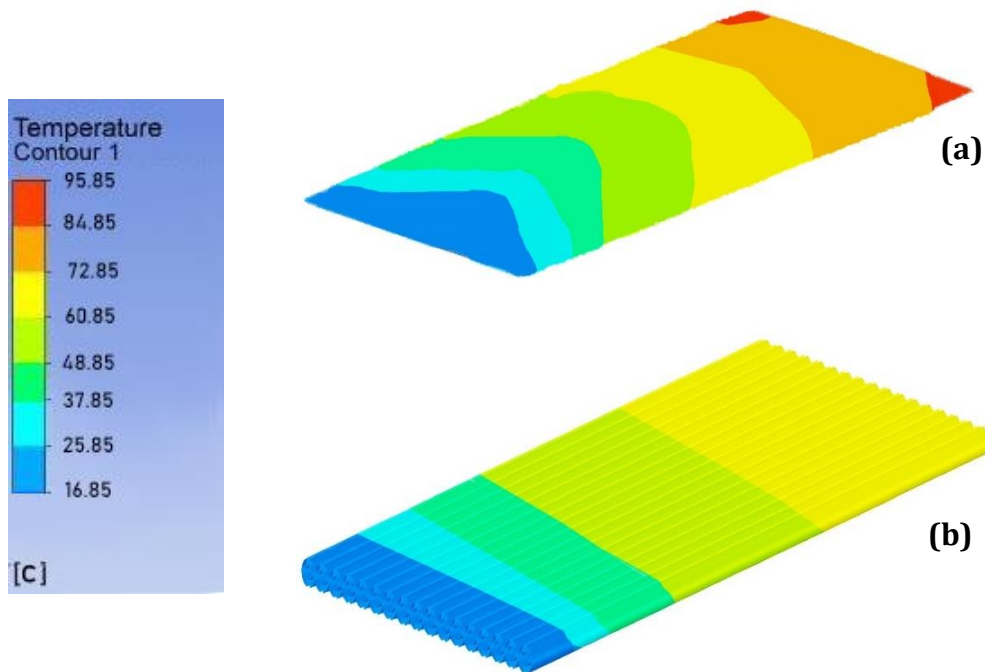


**Figure 10.** Absorber temperature at 0.052 kg/s air flow rate of (a) FSAH and (b) TSAH.

**Figs. 11 to 13** represent the temperature contours of the flowing air through the three SAHs after the simulation at noon. The figures explain the growth of temperature contours of the flowing air. At the FPSAH, the growth of any contour arises from the absorber plate, which is the heating source, and rises upwards to include the upper air layers gradually.

At the TSAH, temperature contours occur at the boundary layer adjacent to the tubes, so heat is transferred from the absorber to the air via a larger area compared to the flat absorber. That difference gives a higher outlet air temperature at the TSAH in comparison to the FPSAH. It is observed from the behavior of the temperature contours that the high absorber temperature of the FPSAH was accompanied by low outlet air temperature in comparison to the TSAH, and vice-versa, the lower absorber temperature of the TSAH was accompanied by higher outlet air temperature in comparison to the FPSAH.

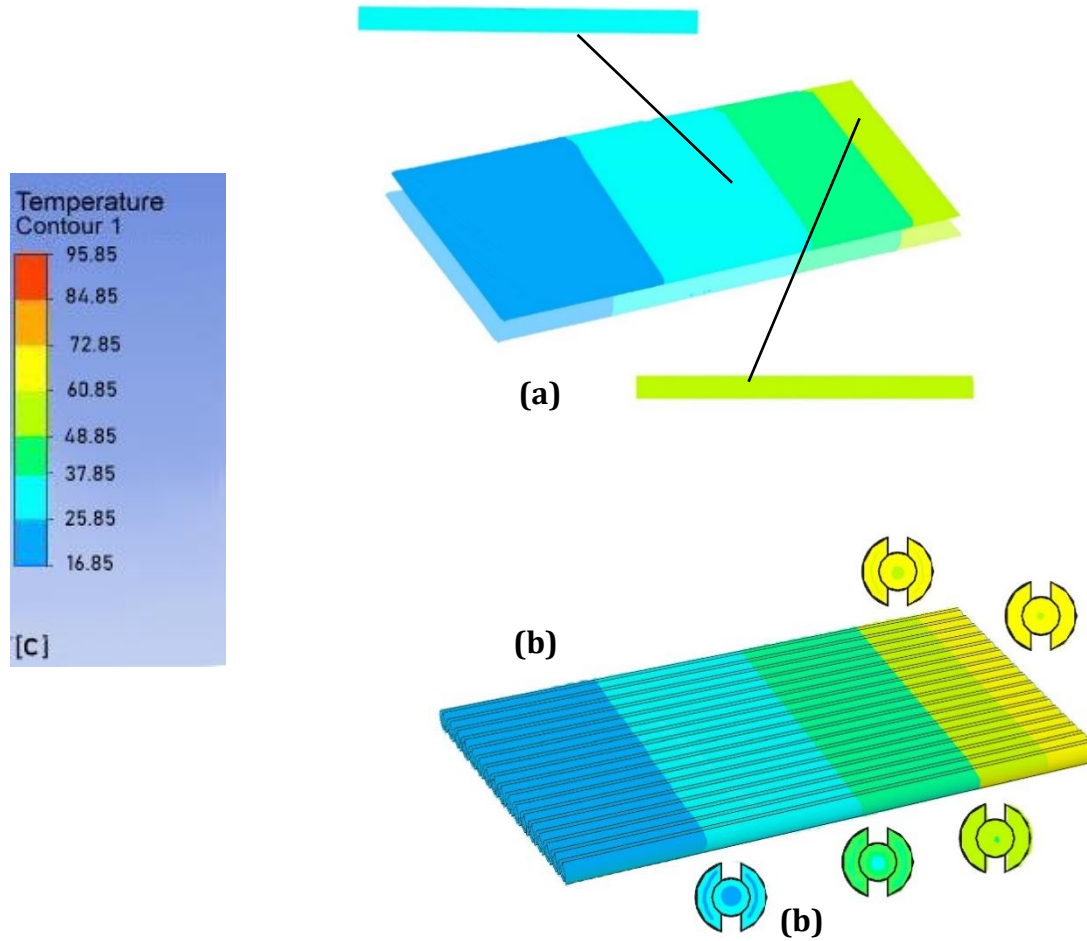


**Figure 11.** Air temperature contours at 0.012 kg/s air flow rate of (a) FSAH and (b) TSAH.

**Figs. 14 and 15** summarize the relation between air flow rate with the absorbers and outlet air temperatures for the two testes heaters. The highest absorber temperature was measured at the FSAH of 90 °C at 0.012 kg/s. The highest outlet air temperature was measured at the TSAH of 58 °C at 0.012 kg/s.

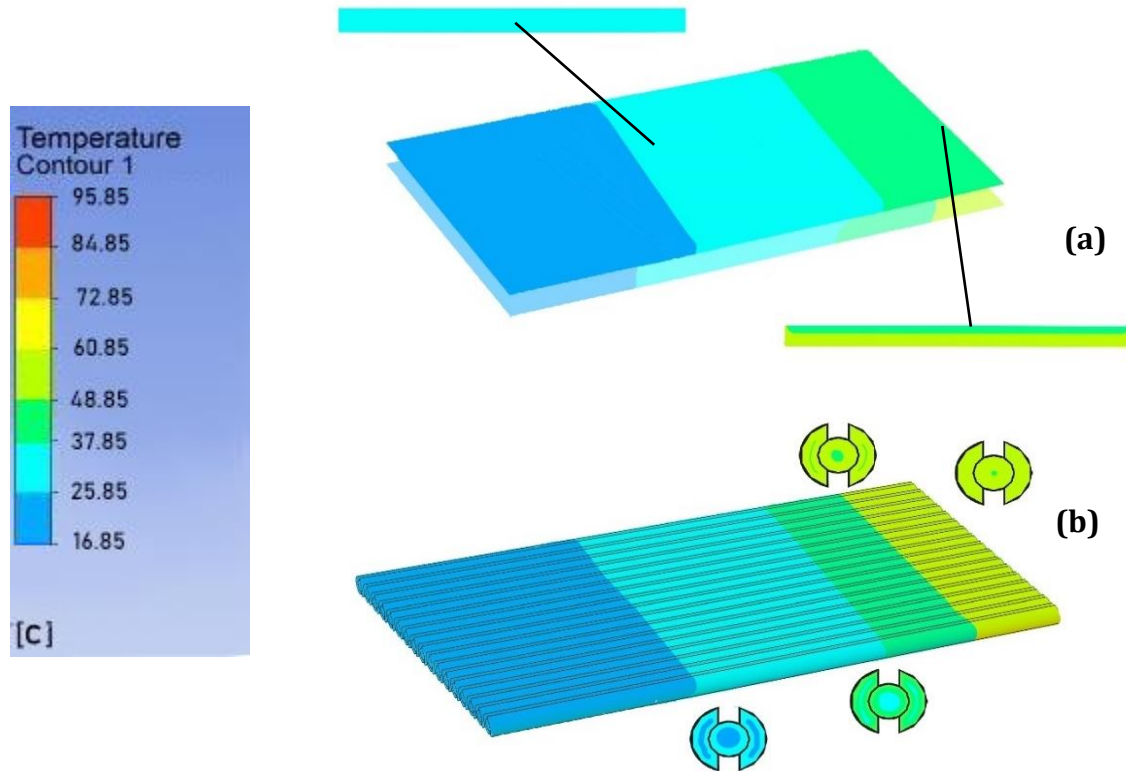


**Figure 12.** Air temperature contours at 0.032 kg/s air flow rate of (a) FSAH and (b) TSAH.

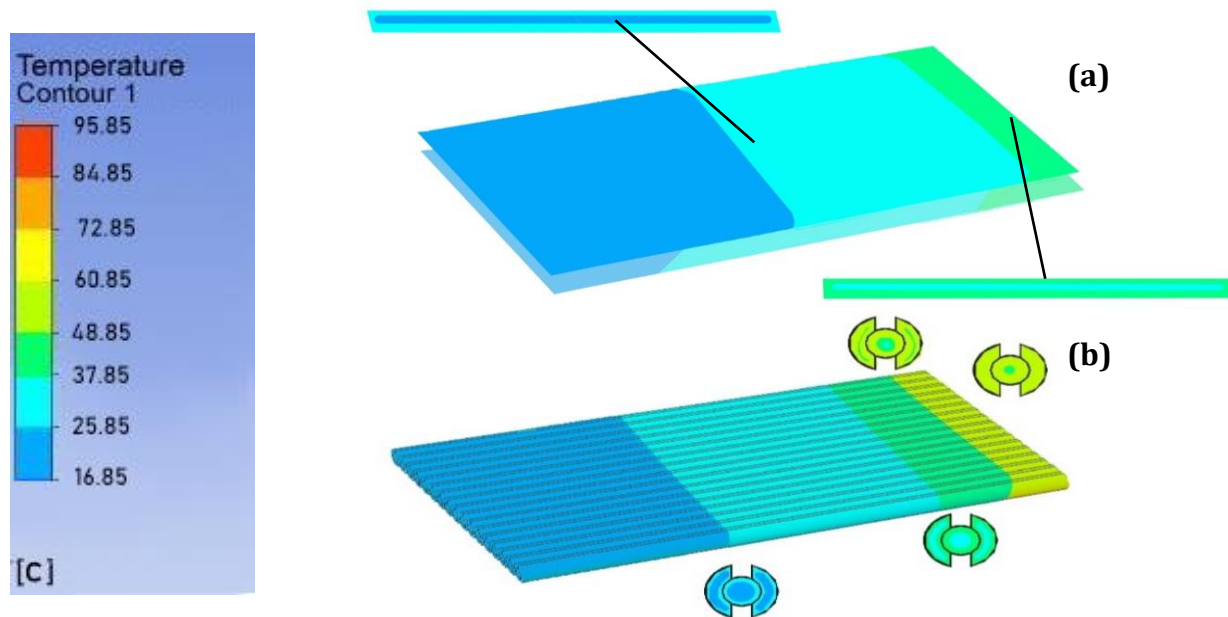


**Figure 13.** Air temperature contours at 0.052 kg/s air flow rate of (a) the FSAH, (b) TSAH

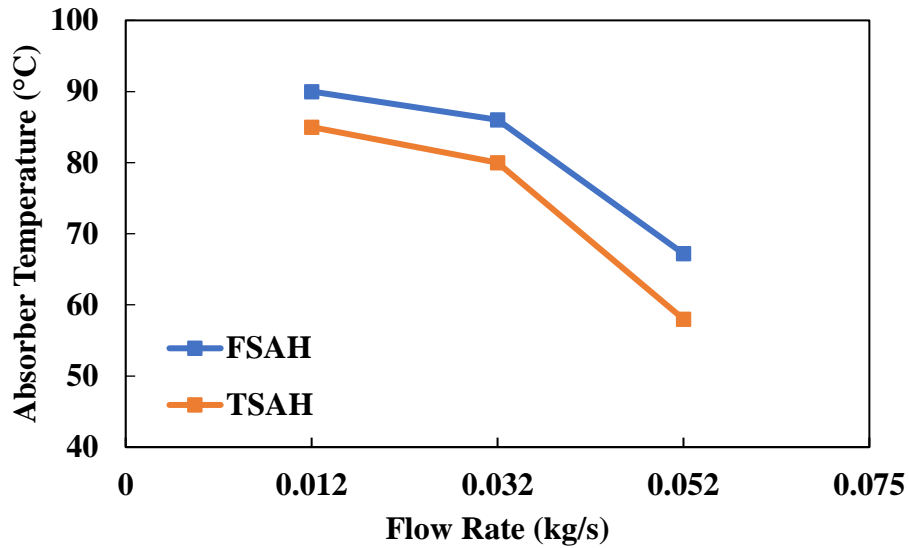


Figure 14. Absorber Temperature

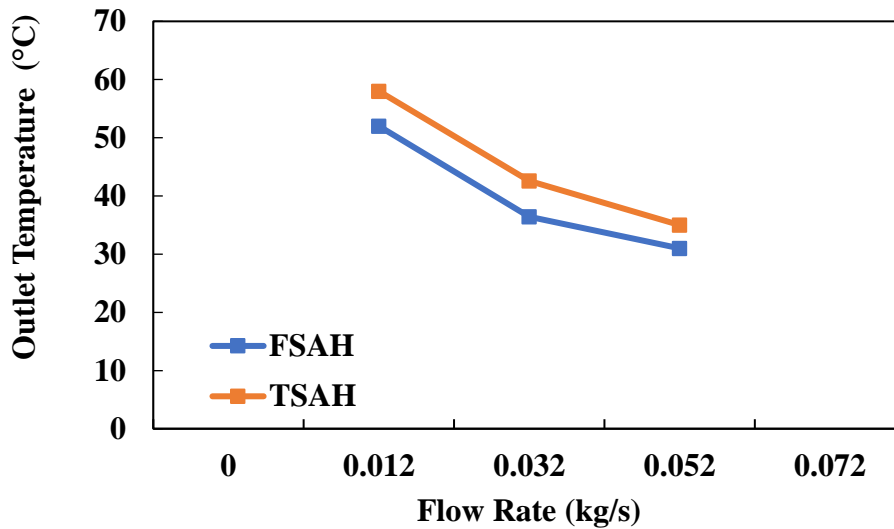


Figure 15. Variation of outlet Air temperature with flow rate

Fig. 16 shows the temperature difference of air through each tested SAH. The highest temperature difference was measured at the TSAH of 38 °C at 0.012 kg/s. It is noticeable that the TSAH gives a temperature difference higher than the FSAH as long as the TSAH works on heating the flowing air through it higher than the FPSAH by 67 W, 207 W, and 222 W at 0.012 kg/s, 0.032 kg/s, and 0.052 kg/s respectively as shown in Fig. 17; As a final result, the TSAH has an excellency of higher thermal efficiency in comparison to the FSAH as demonstrated in Fig. 18. It is noticeable that increasing air flow rate works on cooling the absorber of any SAH, making air able to absorb more heat and more efficient, also, the increment of air flow rate increases the difference of air thermal power and thermal efficiency between the two tested heaters.

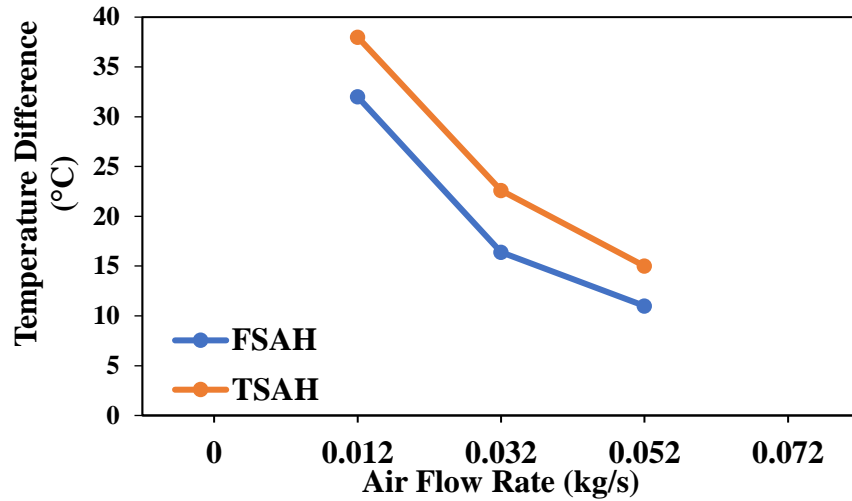


Figure 16. Air temperature difference between inlet and outlet ports of each SAH.

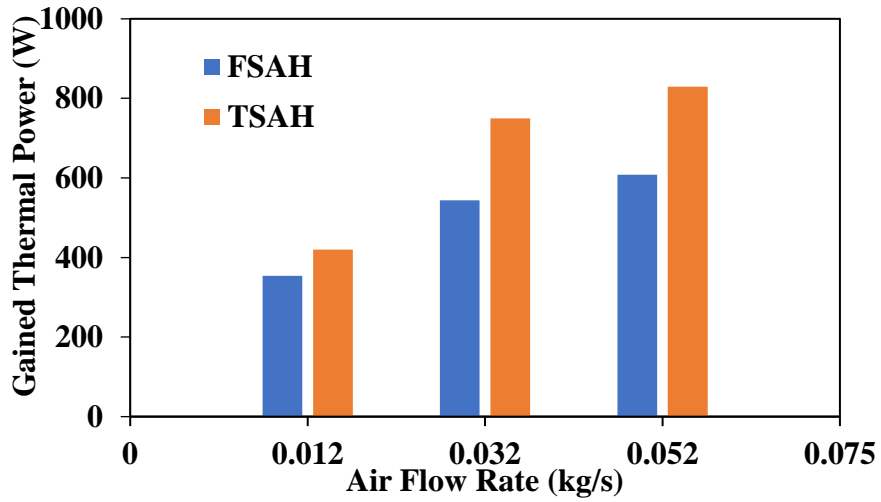


Figure 17. Air thermal power.

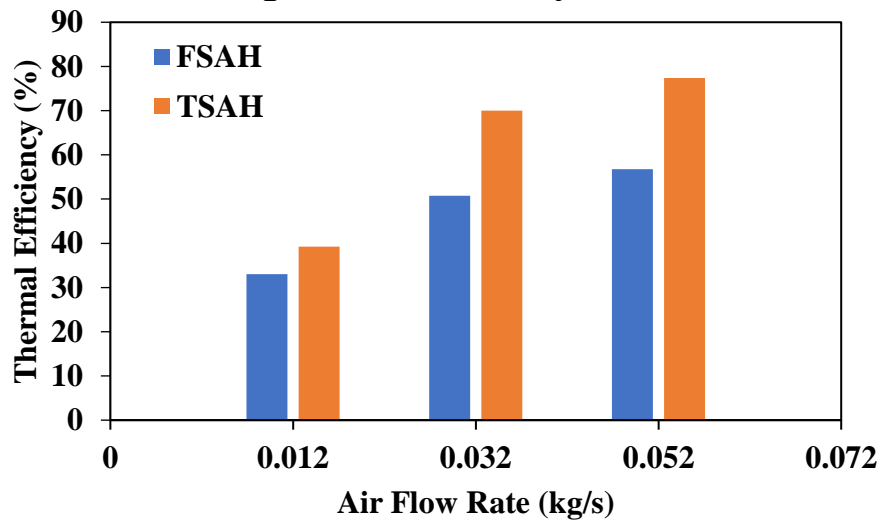


Figure 18. The Thermal efficiency.

## 12. MATHEMATICAL MODEL VALIDATION

A comparison between the present numerical work and (Midhat and Aljubury, 2023) was accomplished for the current numerical model validation. The compared paper tested the behavior of air within the tested SAHs experimentally at the same characteristics considered in the present numerical model. The comparison concluded a close daily thermal efficiency between the researchers, as shown in Figs. 19 and 20 for the flat and tubular absorbers cases, respectively. The difference in the results with the reviewed paper belongs to the assumptions considered in each work.

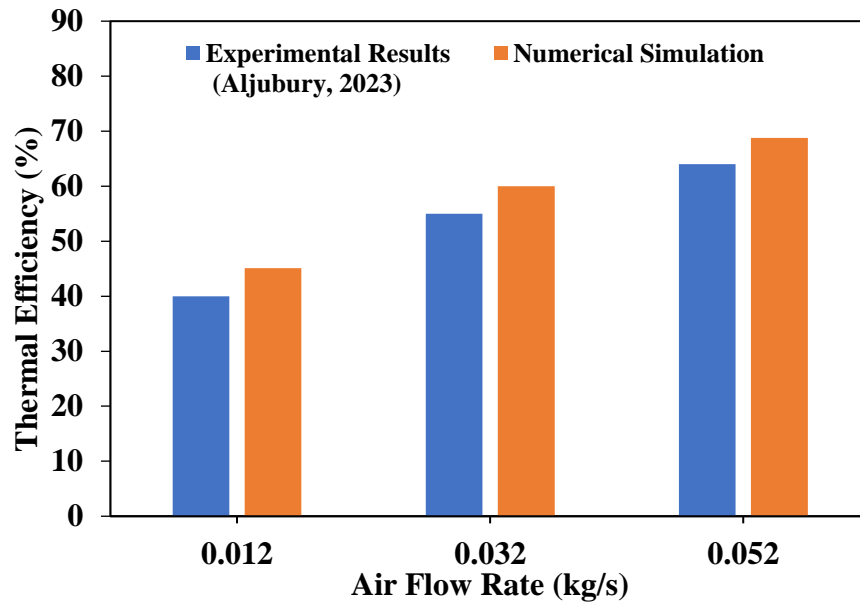


Figure 19. Validation of the FSAH.

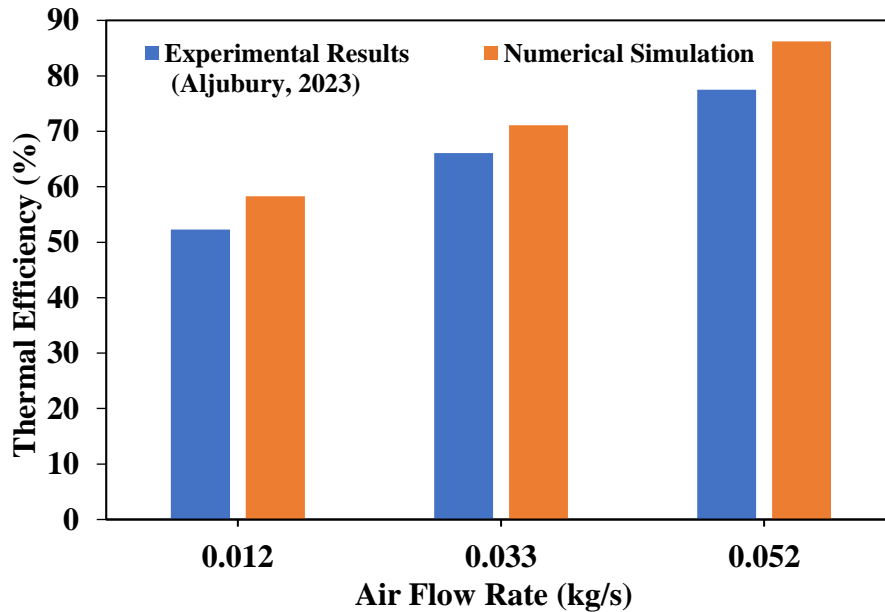


Figure 20. Validation of the TSAH.



### 13. CONCLUSIONS

Airflow through two SAHs, tubular and flat, was simulated using ANSYS-FLUENT 16.0. The simulation was carried out on December 1st. Environmental conditions of the test of 20°C ambient temperature and 1050 W/m<sup>2</sup> solar irradiation were measured experimentally. The main aim of the simulated designs was to investigate the improvement in the thermal performance of the TSAH before manufacturing the SAHs experimentally. Heated air can be utilized in industrial and domestic applications. The conclusion of the investigation can be summarized below:

- The absorber temperature of the FSAH is higher than that of the TSAH, and vice versa. The outlet air temperature of the TSAH is higher than that of the FSAH. That variation can be referred to as the enhancement in heat transfer between the absorber and the flowing air of the TSAH in comparison to the FSAH.
- The TSAH is better than the FSAH in heating air since air is in contact with a larger surface area of the tubes in the case of the TSAH, compared to the contact area between air and the flat plate of the FSAH.
- The highest absorber temperature was measured at the FSAH of 58 °C at 0.012 kg/s.
- The highest outlet air temperature was measured at the TSAH of 90 °C at 0.012 kg/s.
- The highest temperature difference was measured at the TSAH of 38 °C at 0.012 kg/s.
- Increasing airflow can increase the gained thermal power and the thermal efficiency due to the enhancement in heat transfer between the absorber and the flowing air. The best thermal performance was obtained from the TSAH at 0.052 kg/s when the gained thermal power reached 830 W, with about 77 % thermal efficiency.

### NOMENCLATURE

Symbol	Description	Symbol	Description
$\dot{m}$	Mass Flow Rate of the Passing Air (kg/s).	$\nu_t$	kinematic turbulent viscosity (m <sup>2</sup> /s),
$A_{abs}$	Area of the Absorber's Surface (m <sup>2</sup> ).	$\mu_t$	Turbulence Eddy Viscosity (m <sup>2</sup> /s).
$K'$	Turbulence Kinetic Energy (W).	$\epsilon$	Turbulence Dissipation Rate (m <sup>2</sup> /s <sup>3</sup> ).
$Q_{gain}$	Heat gain (W).	$\nu$	kinematic viscosity (m <sup>2</sup> /s),
$Pr$	Prandtl number.	$\Delta T$	Temperature Difference of air Between Inlet and Outlet Ports (°C).
$T$	Temperature (K).	$\epsilon$	Emissivity.
$K$	Thermal Conductivity (W/m. K).	$\eta_{th}$	Thermal Efficiency.
$V$	Velocity of air Within the SAH (m/s).	$\sigma$	Surface tension (N/m).
$I$	Solar irradiation (W/m <sup>2</sup> ).	$\mu$	Viscosity (Pa.s).
$Q_{in}$	Incident Thermal Power (W).	$\rho$ :	Density (kg/m <sup>3</sup> ).

### REFERENCES

Al-Alawy, A.F., Al-Abod, E.E., and Kadhim, R.M., 2018. Numerical simulation of thermal-hydrodynamic behavior within solar air collector. *Journal of Engineering*, 2019(16), pp. 2597–2603. [Doi:10.31026/j.eng.2018.03.03](https://doi.org/10.31026/j.eng.2018.03.03).



- Amori, K.E., and Zghair, F.A., 2019. Evaluation of flat shallow cavity solar collector inserted with porous layer. *The Iraqi Journal for Mechanical and Materials Engineering*, 19(4), pp. 321–336. [Doi:10.32852/ijfmme.v19i4.426](https://doi.org/10.32852/ijfmme.v19i4.426)
- Ammari, H.D., 2003. A mathematical model of thermal performance of a solar air heater with slats. *Renewable Energy*, 28(10), pp. 1597–1615. [Doi:10.1016/S0960-1481\(02\)00253-7](https://doi.org/10.1016/S0960-1481(02)00253-7)
- Çengel, Y.A. 2004. *Thermodynamics: An Engineering Approach*. In McGraw-Hill.
- Duffie, J.A., and Beckman, W.A., 1985. *Solar Engineering of Thermal Processes*. Wiley
- Farhan, A. A., and Sahi, H. A. 2017. Energy analysis of solar collector with perforated absorber plate. *Journal of Engineering*, 23(9), pp. 89–102. [Doi:10.1016/j.renene.2021.01.109](https://doi.org/10.1016/j.renene.2021.01.109)
- Hammadi, M.A., 2015. Numerical analysis of fluid flow and heat transfer by forced convection in channel with one-sided semicircular sections and filled with porous media mouwaffaq. *Journal of Engineering*, 21(5), pp. 1–21. [Doi:10.31026/j.eng.2015.05.01](https://doi.org/10.31026/j.eng.2015.05.01)
- Hasan, H.A., 2017. Thermal Performance Enhancement of Phase Change Materials (PCMs) by Using Metal Foams. *Al-Nahrain Journal for Engineering Sciences (NJES)*, 20(1), pp 235–249. <https://nahje.com/index.php/main/article/view/91>
- Hasan, H.A., and Hussain, I.Y., 2018. Theoretical formulation and numerical simulation of thermal performance enhancements for cascade thermal energy storage systems. *IOP Conference Series: Materials Science and Engineering*, 433(1), pp 235-249. [Doi:10.1088/1757-899X/433/1/012043](https://doi.org/10.1088/1757-899X/433/1/012043)
- Heydari, A., and Mesgarpour, M., 2018. Experimental analysis and numerical modeling of solar air heater with helical flow path. *Solar Energy*, 162, pp. 278–288. [Doi:10.1016/j.solener.2018.01.030](https://doi.org/10.1016/j.solener.2018.01.030)
- Hussain, I.Y., and Mustafa, A.W., 2010. Investigation of the effect of the wake generated by rotor blades on the flow through stator passage for low pressure turbine. 16(2). *Journal of Engineering*. 16(2), pp. 5098-5115. Doi????
- Al-Abbas, A.H., 2017. Computational Fluid Dynamics (CFD) modeling study of thermal performance for multipurpose solar heating system. *Al-Nahrain Journal for Engineering Sciences (NJES)*, 20(1), pp. 222–234. <https://www.iasj.net/iasj/download/3eaf9d1381773c05>
- Hussein, N.F., Ahmed, S.T., and Ekaid, A.L., 2023. Thermal performance of double pass solar air heater with tubular solar absorber. *International Journal of Renewable Energy Development*, 12(1), pp. 11–21. [Doi:10.14710/ijred.2023.46328](https://doi.org/10.14710/ijred.2023.46328)
- Yasin, N.J., and Ghanim, A.H., 2017. Assessment for heat transfer enhancement in heat exchangers by using dimples geometry. *Association of Arab Universities. Journal of Engineering Sciences*, 24(2), pp. 44–67. <https://jaaru.org/index.php/auisseng/issue/view/2>.
- Jassim, N.A., and Shbailat, S.J., 2017. Three-dimensional CFD analysis for simulating dual channel solar collector with different absorbing media. *International Journal of Thermal Technologies*, 10(January). pp. <http://doi.org/10.102277-4114.inpressco.com/ijtt>



- Jassim, N.A., Shbailat, S.J., 2018. Energy and exergy analysis of dual channel solar air collector with different absorber plates geometry. *Journal of Engineering*, 2019(16), pp. 2597–2603. <https://digital-library.theiet.org/10.1049/joe.2018.8601>
- Jehhef, K. A., 2018. Numerical simulation of flow in rectangular duct with different obstruction heights. *Journal of Engineering*, 21, pp. 94-110 .[Doi:10.31026/j.eng.2015.11.06](https://doi.org/10.31026/j.eng.2015.11.06)
- Jin, D., Quan, S., Zuo, J., and Xu, S., 2019. Numerical investigation of heat transfer enhancement in a solar air heater roughened by multiple V-shaped ribs. *Renewable Energy*, 134, pp. 78–88. [Doi:10.1016/j.renene.2018.11.016](https://doi.org/10.1016/j.renene.2018.11.016)
- Jouybari, N.F., and Lundström, T.S., 2020. Performance improvement of a solar air heater by covering the absorber plate with a thin porous material. *Energy*, 190, pp. 1-29. [Doi:10.1016/j.energy.2019.116437](https://doi.org/10.1016/j.energy.2019.116437)
- Kadhim, A. F., and Al Thamiry, H. A., 2021. Numerical simulation to investigate the occurrence of vortices at double vertical pumps intakes. *Association of Arab Universities Journal of Engineering Sciences*, 28(1), pp. 01–06. [Doi:10.33261/jaaru.2021.28.1.001](https://doi.org/10.33261/jaaru.2021.28.1.001)
- Khanlari, A., Güler, H.Ö., Tuncer, A.D., Şirin, C., Bilge, Y.C., Yılmaz, Y., and Güngör, A., 2020. Experimental and numerical study of the effect of integrating plus-shaped perforated baffles to solar air collector in drying application. *Renewable Energy*, 145, pp. 1677–1692. [Doi:10.1016/j.renene.2019.07.076](https://doi.org/10.1016/j.renene.2019.07.076)
- Kundan, K. 2017. Mathematical modelling and optimization of solar air heater using CFD. *International Journal for Research in Applied Science and Engineering Technology*, V(IX), pp. 1341–1350. [Doi:10.22214/ijraset.2017.9192](https://doi.org/10.22214/ijraset.2017.9192)
- Midhat, Y.F., and Aljubury, I.M.A., 2023. Experimental evaluation of thermohydraulic performance of tubular solar air heater. *International Journal of Renewable Energy Development*, 12(1), pp. 66–76. [Doi:10.14710/ijred.2023.45312](https://doi.org/10.14710/ijred.2023.45312)
- Nasir, K.F., 2019. Thermal Performance of Plastic Receiver in Solar Collector. *Journal of Engineering*, 25(7), pp. 37–60. [Doi:10.31026/j.eng.2019.07.03](https://doi.org/10.31026/j.eng.2019.07.03)
- Nakhla, D., 2013. An Enhanced Latent Heat Thermal Storage System Using Electrohydrodynamics (EHD). *Journal of McMaster University*, pp. 1-181. [Doi:10.31026/j.eng.2015.05.10`](https://doi.org/10.31026/j.eng.2015.05.10)
- Olczak, P., and Olek, M., 2016. The Influence of Evacuated-tube Collector Assembly on Heat Loss in Tracking Solar System with Parabolic Mirror Reflectors. *Procedia Engineering*, 157, pp. 317–324. [Doi:10.1016/j.proeng.2016.08.372](https://doi.org/10.1016/j.proeng.2016.08.372)
- Raj, A.K., Srinivas, M., and Jayaraj, S. 2020. Transient CFD analysis of macro-encapsulated latent heat thermal energy storage containers incorporated within solar air heater. *International Journal of Heat and Mass Transfer*, 156, P. 119896. [Doi:10.1016/j.ijheatmasstransfer.2020.119896](https://doi.org/10.1016/j.ijheatmasstransfer.2020.119896)
- Sahu, M.K., and Prasad, R.K., 2017. Thermohydraulic performance analysis of an arc shape wire roughened solar air heater. *Renewable Energy*, 108, pp. 598–614. [Doi:10.1016/j.renene.2017.02.075](https://doi.org/10.1016/j.renene.2017.02.075)
- Salih, S.M., Jalil, J.M., and Najim, S.E., 2020. Comparative study of novel solar air heater with and without latent energy storage. *Journal of Energy Storage*, 32, 101751, pp. 1-14 [Doi:10.1016/j.est.2020.101751](https://doi.org/10.1016/j.est.2020.101751)



- Salih, S., and Najim, S., 2019. Numerical modeling for novel solar air heater utilizing wax paraffin-PCM. *Basrah Journal for Engineering Science*, 19(2), pp. 1–8. [Doi:10.33971/bjes.19.2.1](https://doi.org/10.33971/bjes.19.2.1)
- Salman, A.S., and Nima, M.A., 2019. Numerical study of fluid flow and heat transfer characteristics in solid and perforated finned heat sinks utilizing a piezoelectric fan. *Journal of Engineering*, 25(7), pp. 83–103. [Doi:10.31026/j.eng.2019.07.05](https://doi.org/10.31026/j.eng.2019.07.05)
- Kalogirou S.A., 2014. *Solar Energy Engineering: Processes and Systems*. 2nd Edition, Fisicalbook
- Shbailat, S., and Jassim, N., 2018. Energy and exergy analysis of dual channel solar air collector with perforating “V” corrugated absorber plate. *Basrah Journal for Engineering Science*, 18(1), pp. 10–15. [Doi:10.33971/bjes.18.1.2](https://doi.org/10.33971/bjes.18.1.2)
- Singh, S., 2020. Experimental and numerical investigations of a single and double pass porous serpentine wavy wiremesh packed bed solar air heater. *Renewable Energy*, 145, pp. 1361–1387. [Doi:10.1016/j.renene.2019.06.137](https://doi.org/10.1016/j.renene.2019.06.137)
- Tuncer, A.D., Khanlari, A., Sözen, A., Gürbüz, E.Y., Şirin, C., and Gungor, A., 2020. Energy-exergy and enviro-economic survey of solar air heaters with various air channel modifications. *Renewable Energy*, 160, pp. 67–85. [Doi:10.1016/j.renene.2020.06.087](https://doi.org/10.1016/j.renene.2020.06.087)
- Varol, Y., and Oztop, H.F., 2008. A comparative numerical study on natural convection in inclined wavy and flat-plate solar collectors. *Building and Environment*, 43(9), pp. 1535–1544. [Doi:10.1016/j.buildenv.2007.09.002](https://doi.org/10.1016/j.buildenv.2007.09.002)
- Yasin, N.J., and Suliman, D., 2015. Heat transfer characteristics of a fluid flow in multi tube heat exchanger fitted with perforated fins. *Journal of Engineering*, 21(11), pp. 40–59. [Doi:10.31026/j.eng.2015.11.03](https://doi.org/10.31026/j.eng.2015.11.03)